European Journal of Nuclear Medicine and Molecular Imaging

Supplementary Material for "Individual-level metabolic connectivity from dynamic [^{18}F]FDG PET reveals glioma-induced impairments in brain architecture and offers novel insights beyond the SUVR clinical standard"

Giulia Vallini, Erica Silvestri†, Tommaso Volpi†, John J. Lee, Andrei G. Vlassenko, Manu S. Goyal, Diego Cecchin, Maurizio Corbetta and Alessandra Bertoldo

†**These authors contributed equally to this work.**

Corresponding author: Alessandra Bertoldo
Department of Information Engineering, University of Padova, Padova, Italy
Padova Neuroscience Center, University of Padova, Padova, Italy
E-mail: bertoldo@dei.unipd.it
https://orcid.org/0000-0002-6262-6354

Materials and methods

Participants

Pre-surgical data of 44 patients (mean age 60.8 ± 14.9 years, 25 males) with *de novo* glioma, were collected at the University Hospital of Padova between June 2016 and April 2021. The healthy control (HC) group was composed of 57 adults (mean age 55.8 ± 15.2 years, 25 males) as part of the Adult Metabolism & Brain Resilience (AMBR) study [1].

Data acquisition

Patient data were acquired on a 3T Siemens Biograph PET/MR scanner. Anatomical images comprised a T1-weighted (T1w) 3D magnetization-prepared rapid gradient-echo acquisition (TR=2400 ms, TE=3.24 ms, TI=1000 ms, FA=8°, FOV=256×256 mm, voxel size=1×1×1 mm^3) acquired both before and after contrast agent injection, a 3D T2-weighted image (TR=3200 ms, TE=535 ms, FOV=256×256 mm, voxel size=1×1×1 mm^3) and a 3D fluid

attenuation inversion recovery image (TR=5000 ms, TE=284 ms, TI=1800 ms, FOV=256×256 mm, voxel size=1×1×1 mm^3). Dynamic PET acquisitions (60-minute acquisition) were performed following an intravenous bolus manual injection of 203 ± 40 MBq and images were reconstructed using the OSEM algorithm starting from list-mode data.

For each HC, a structural MRI scan was acquired on a Siemens Magnetom $Prisma^{fit}$ scanner, with a 3D sagittal T1-weighted magnetization-prepared 180° radio-frequency pulses and rapid gradient-echo multi-echo sequence (TE = 1.81, 3.6, 5.39, 7.18 ms, TR = 2500 ms, TI = 1000 ms and voxels size of 0.8×0.8×0.8 mm^3). The final T1-weighted image was obtained by averaging the first two echoes [2]. Dynamic PET acquisitions (60-minute acquisition) were performed following an intravenous bolus manual injection of 187.7 ± 12.1 MBq and reconstructed by filtered back-projection (ramp filter, 5 mm FWHM).

In both patients and controls, the injection and subsequent saline flush lasted less than 30 seconds.

MRI preprocessing

Imaging data from patients and healthy controls underwent similar structural pre-processing with an in-house pipeline. T1w structural images were N4 bias field-corrected [3], skull-stripped [4], and segmented into grey matter (GM), white matter (WM) and cerebrospinal fluid (CSF) using the Statistical Parametric Mapping 12 (SPM12 v. 7219 https://www.fil.ion.ucl.ac.uk/spm/).

A threshold of 0.8 was applied to these probability maps to generate binary masks for GM, WM, and CSF. Specifically, the binary GM mask is utilized for extracting time-activity curves (TACs) of voxels, therefore the chosen segmentation is intentionally conservative, resulting in a mean sample TAC that effectively reduces partial volume effects (PVEs) [5], while still maintaining a sufficient number of voxels. On the other hand, to create the reference region mask for standardized uptake value ratio (SUVR) calculation, the binary mask for WM was applied to the cerebellum region (defined according to the Hammers atlas).

T1w images were normalized to the FSL's MNI152 standard space by nonlinear diffeomorphic registration using the Advanced Normalization Tools (ANTs v. 2.4.3) [6]. Hammers' anatomical atlas [7], and Yan's functional atlas (100 ROIs, 7 networks [8]) were registered in T1w space by inverting the obtained nonlinear transformation. In the patient group, all normalizations done with ANTs were performed excluding the TM+E area [9].

Within-individual metabolic connectivity

Within-individual metabolic connectivity (wi-MC) matrices were calculated using a method based on Euclidean Similarity (ES), detailed in Volpi et al. [10]. For each pair of TACs, z_1 and z_2, their Euclidean distance $d_{z1,z2}$ is calculated:

$$d_{z1,z2} = \sqrt{\sum_{i=1}^{T}(z_{i,1} - z_{i,2})^2} \qquad \text{with } T = \text{number of time points} \tag{1}$$

A measure of ES is obtained as 1 minus the normalized $d_{z1,z2}$, i.e., divided by the maximum distance between TAC pairs (scaled in the [0, 1] interval). Due to the heavy-tailed distribution of the ES values, a Fisher z-transformation was applied, followed by a new rescaling of the values in the [0, 1] interval. A wi-MC matrix was calculated for all participants, both HCs and patients.

Thresholds sensitivity

With the aim to assess the thresholds' impact on defining altered regions, we conducted a sensitivity analysis for both the estimation of wi-MC and SUVR impairments.

For wi-MC, thresholds corresponding to the 95.5th, 96.5th, 97.5th, and 98.5th percentiles of the DfHG index reference distribution in healthy controls were tested. For each threshold, a binary matrix with the altered regions for each patient was generated, and Dice coefficients were computed between the matrices from different thresholds.

A similar procedure was employed to test the threshold sensitivity for SUVR alterations. Specifically, for each region, the two thresholds of hypo- and hyper-metabolism were defined on the healthy control distribution, encompassing 95.5%, 96.5%, 97.5% and 98.5% of the values. Binary matrices with the SUVR alterations for each patient were generated, and Dice coefficients were computed between the matrices from different thresholds.

Finally, for each corresponding threshold, we computed the Dice coefficient between the wi-MC alteration matrix and the corresponding SUVR alteration matrix to assess the threshold sensitivity of the overlap.

SUVR impairments

The degree of alteration in each region in terms of SUVR was defined as the absolute difference between the value of the patient's ROI and the mean of the SUVR values distribution for the same ROI in the healthy group (distributions are normal, as confirmed by

the Lilliefors test). Subsequently, the Overall Impairment (OI) for each patient was calculated as the average of the DfHG values across all ROIs. We then investigated the across-individual association between OI and tumor grade, as well as the volume of both the entire lesion (TM+E) and the tumor (TM). Specifically, the Mann-Whitney U-test ($P < 0.05$) was employed to compare the OI between patients with HGG and LGG, while a linear regression analysis was performed to assess the relationship of OI with TM+E and TM volume.

Impact of scanner and reconstruction algorithm

We conducted a preliminary assessment to evaluate the potential impact of employing distinct scanners and reconstruction algorithms for the two datasets (patients and controls). Specifically, the Contrast-to-Noise ratio (CNR) was calculated for each participant in both groups (HCs and patients) as the ratio of mean PET signal in GM to mean PET signal in WM from the generated static PET images (40-60 min). This portion of the PET signal was chosen because it is the one from which SUVRs are calculated, and because the structure of wi-MC matrices, as obtained with the Euclidean Similarity method, is mainly dependent on the tail of the time-activity curves (40-60 min) [10]. Finally, the two distributions were compared by means of the Mann-Whitney U-test ($P < 0.05$).

List of Hammers ROIs

Left hemisphere

Subcortical

1. Cerebellum
2. Caudate nucleus
3. Nucleus accumbens
4. Putamen
5. Thalamus
6. Pallidum

Frontal

7. Middle frontal gyrus
8. Precentral gyrus
9. Straight gyrus
10. Anterior orbital gyrus
11. Inferior frontal gyrus

12. Superior frontal gyrus
13. Medial orbital gyrus
14. Lateral orbital gyrus
15. Posterior orbital gyrus
16. Subgenual frontal cortex
17. Subcallosal area
18. Pre-subgenual frontal cortex

Insula & Cingulum

19. Insula
20. Cingulate gyrus (gyrus cinguli), anterior part
21. Cingulate gyurs (gyrus cinguli), posterior part

Temporal

22. Hippocampus
23. Amygdala
24. Anterior temporal lobe, medial part
25. Anterior temporal lobe, lateral part
26. Parahippocampal and ambient gyri
27. Superior temporal gyrus, posterior part
28. Middle and Inferior temporal gyrus
29. Fusiform gyrus
30. Posterior temporal lobe
31. Superior temporal gyrus, anterior part

Parietal

32. Postcentral gyrus
33. Superior parietal gyrus
34. Inferiolateral remainder of parietal lobe

Occipital

35. Lingual gyrus
36. Cuneus
37. Lateral remainder of occipital lobe

Right hemisphere

Subcortical

38. Cerebellum
39. Caudate nucleus

40. Nucleus accumbens
41. Putamen
42. Thalamus
43. Pallidum

Frontal

44. Middle frontal gyrus
45. Precentral gyrus
46. Straight gyrus
47. Anterior orbital gyrus
48. Inferior frontal gyrus
49. Superior frontal gyrus
50. Medial orbital gyrus
51. Lateral orbital gyrus
52. Posterior orbital gyrus
53. Subgenual frontal cortex
54. Subcallosal area
55. Pre-subgenual frontal cortex

Insula & Cingulum

56. Insula
57. Cingulate gyrus (gyrus cinguli), anterior part
58. Cingulate gyurs (gyrus cinguli), posterior part

Temporal

59. Hippocampus
60. Amygdala
61. Anterior temporal lobe, medial part
62. Anterior temporal lobe, lateral part
63. Parahippocampal and ambient gyri
64. Superior temporal gyrus, posterior part
65. Middle and Inferior temporal gyrus
66. Fusiform gyrus
67. Posterior temporal lobe
68. Superior temporal gyrus, anterior part

Parietal

69. Postcentral gyrus

70. Superior parietal gyrus

71. Inferiolateral remainder of parietal lobe

Occipital

72. Lingual gyrus

73. Cuneus

74. Lateral remainder of occipital lobe

Results

Participants

Supplementary Fig. 1 shows the lesion frequency maps in the patient population, calculated from the tumor plus edema (TM+E) mask (**Supplementary Fig. 1a**) and the tumor (TM) mask (**Supplementary Fig. 1b**).

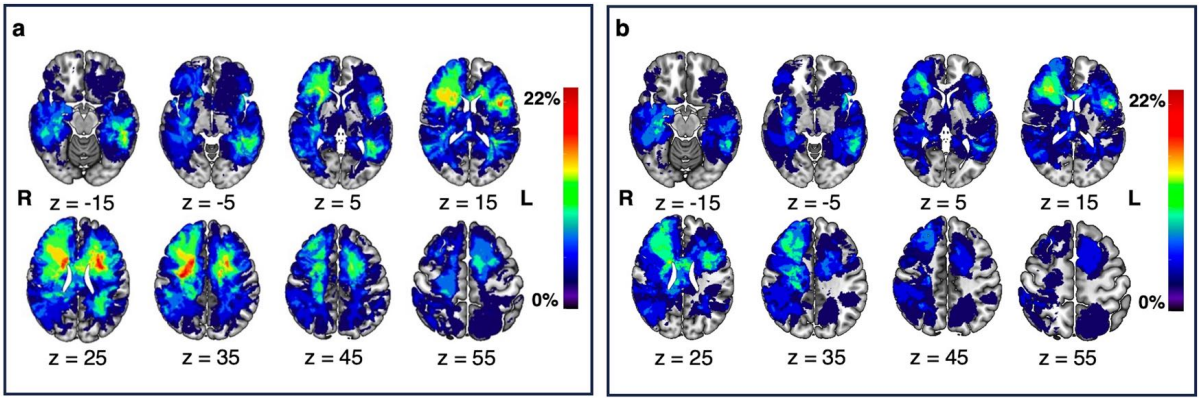

Supplementary Fig. 1 Frequency map (% over total patient number) of (**a**) tumor lesions, including area of edema (TM+E), and (**b**) tumor-only (TM), including tumor core (contrast agent enhancing and non-enhancing regions) and necrosis

Thresholds sensitivity

Supplementary Fig. 2a shows the Dice coefficient values calculated on the wi-MC alteration binary matrices, obtained at different thresholds (95.5^{th}, 96.5^{th}, 97.5^{th}, 98.5^{th} percentiles). **Supplementary Fig. 2b** reports the values of Dice coefficient calculated on the SUVR alteration binary matrices, obtained at different thresholds (95.5%, 96.5%, 97.5%, 98.5%). **Supplementary Fig. 2c** shows, for each threshold, the Dice between corresponding matrices of wi-MC and SUVR alteration.

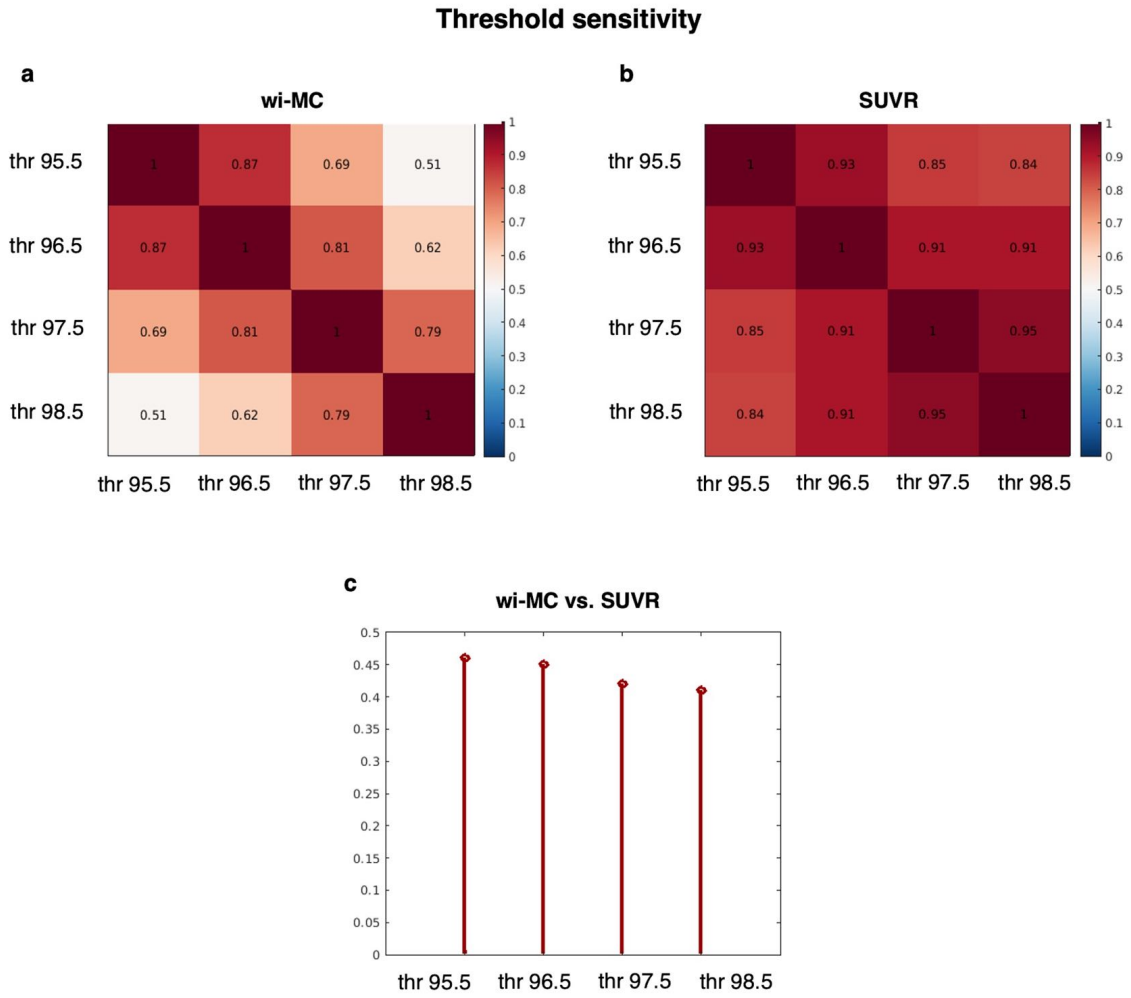

Supplementary Fig. 2 (a) Dice similarity between wi-MC alteration matrices (all patients, all regions) obtained at different thresholds. **(b)** Dice similarity between SUVR alteration matrices (all patients, all regions), obtained at different thresholds. **(c)** Dice similarity between corresponding alteration matrices of wi-MC and SUVR, for each threshold value

SUVR impairments

Supplementary Fig. 3 depicts the relationships of the SUVR Overall Impairment (OI) index (Yan atlas) with the entire lesion (TM+E) volume (**Supplementary Fig. 3a**) and the tumor (TM) volume (**Supplementary Fig. 3b**). In both cases, no significant relationship emerges, while it is evident that patients with low-grade gliomas present less pronounced compromises in local metabolism compared to HGGs. This observation is confirmed via the Mann-Whitney U-test, which revealed HGG patients having a significantly higher OI index than LGG ($P < 0.001$).

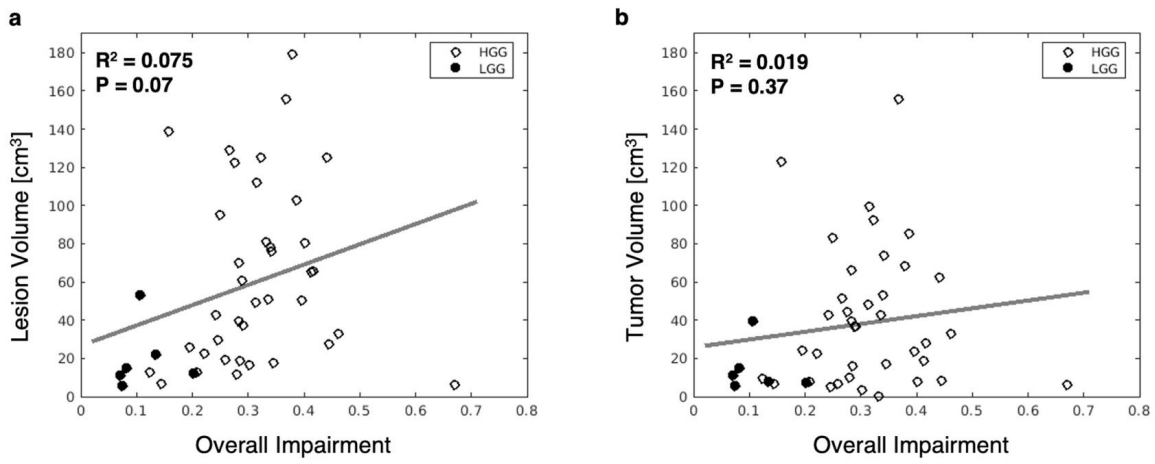

Supplementary Fig. 3 Scatter plots reporting the association between the Overall Impairment index and (**a**) lesion volume (tumor and edema) and (**b**) tumor volume (without edema), on the Yan functional atlas. High-grade glioma (HGG) patients are shown as empty dots, low-grade glioma (LGG) patients as black-filled dots

Impact of scanner and reconstruction algorithm

Supplementary Fig. 4 shows the distributions of the CNR values calculated on the static PET scans (40-60 min) for the two groups (patients and controls). Comparing CNR values using the Mann-Whitney U-test, no significant difference emerged (P = 0.97).

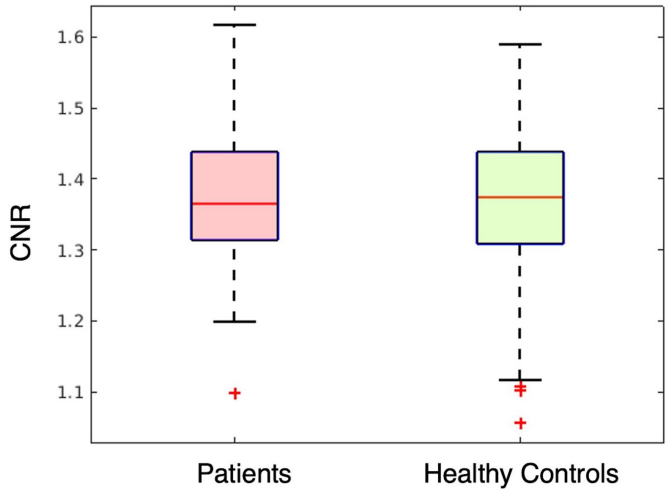

Supplementary Fig. 4 CNR values calculated as the ratio between mean GM and mean WM [^{18}F]FDG uptake in each individual PET image (static PET, 40-60 min) for both population groups (red: patients, green: healthy controls)

Hammers' atlas results

Impairment maps

Supplementary Fig. 5 shows the impairment maps of 4 representative patients. Upon visual inspection, it is evident that in all individuals there are compromised regions that overlap with the lesion areas. However, the compromised ROIs are not limited to the lesioned tissue, with wi-MC alterations extending to uninjured brain areas in both the ipsilateral and contralateral hemispheres, especially in patients with high-grade gliomas (**Supplementary Fig. 5**, patients 7, 12, 24).

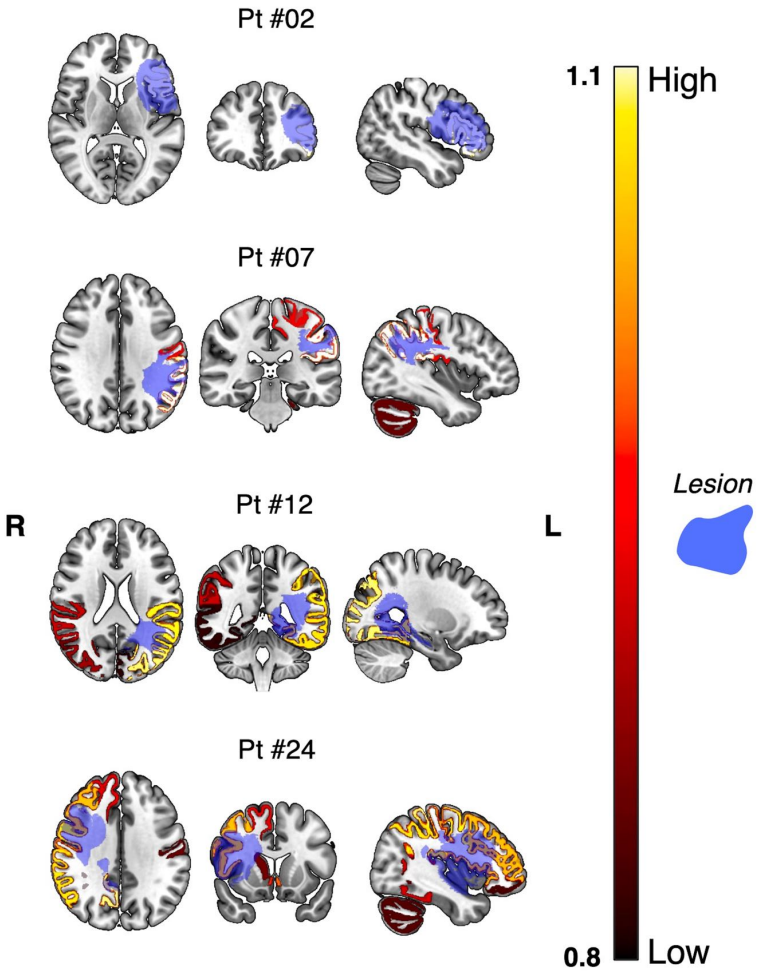

Supplementary Fig. 5 The lesion mask (TM+E) is shown in blue, the altered ROIs (Hammers anatomical atlas, GM-masked) are shown according to their DfHG index value, from low (dark) to high (light). Pt #02 has a low-grade glioma in the left frontal lobe; Pt #07 has a high-grade glioma in the left parietal lobe; Pt #12 has a high-grade glioma in the left temporal lobe and Pt #24 has a high-grade glioma in the right fronto-insular area

SUVR and wi-MC impairments

Supplementary Fig. 6a reports the impaired regions (*rows*), grouped according to the Hammers' anatomical cluster, for each patient (*columns*). The matrix distinguishes between SUVR-only impairments (*green*), wi-MC-only impairments (*orange*), and regions where both SUVR and wi-MC exhibit alterations (*purple*). The complementarity of the alterations highlighted by the network-based and local approach is evident, with a greater overlap in Frontal and Parietal areas (**Supplementary Fig. 6b**).

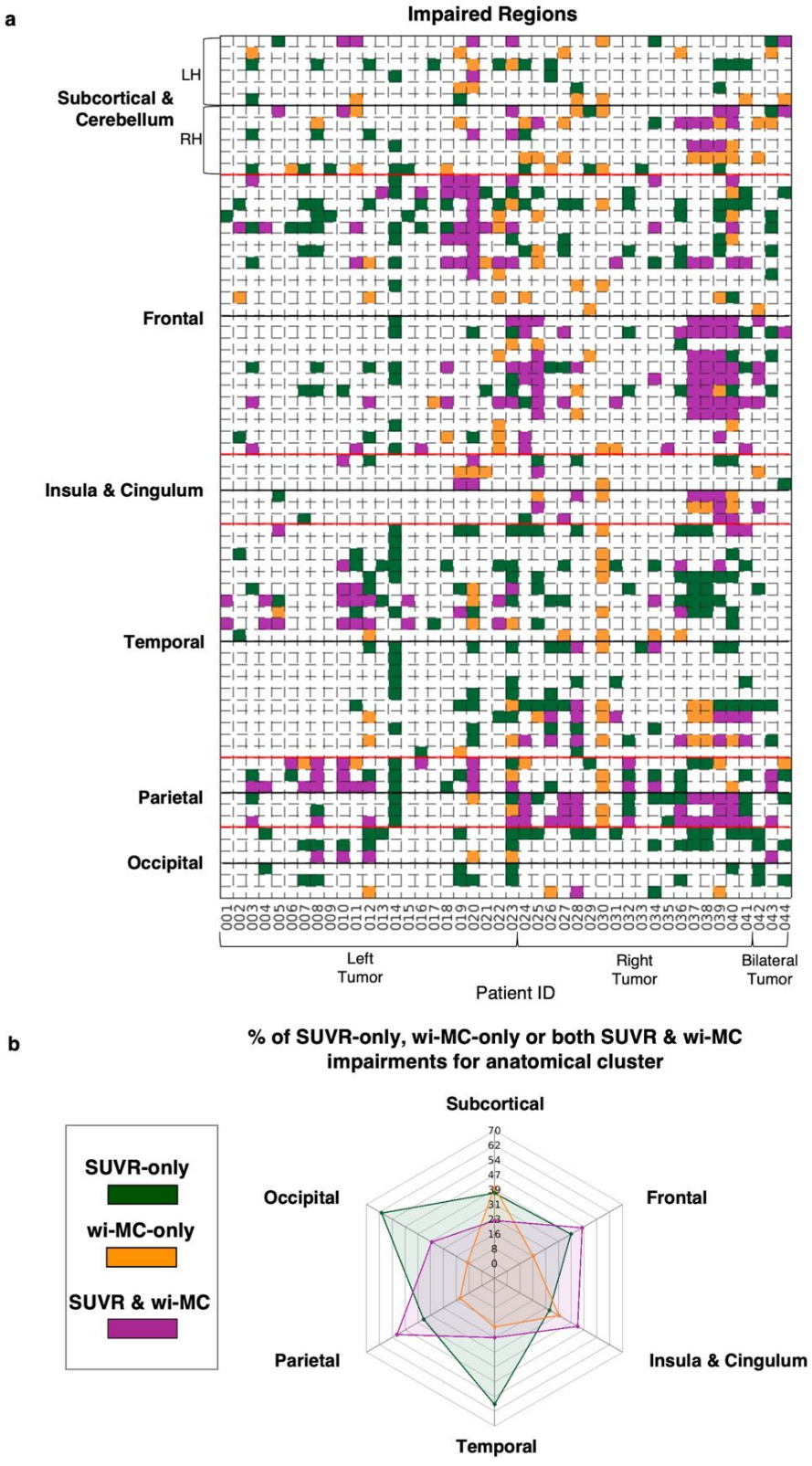

Supplementary Fig. 6 (**a**) Altered regions (Hammers atlas) according to SUVR only (green), wi-MC only (orange), both SUVR and wi-MC (purple) are reported (rows) for each individual patient (columns). Patients are sorted into: patients with lesions in the left hemisphere (Left Tumor), patients with lesions on the right (Right Tumor), and patients with

bilateral lesions (Bilateral Tumor). The regions are organized by anatomical clusters. (**b**) Spider plot representing the percentage of altered regions by type (SUVR-only, wi-MC-only, both SUVR and wi-MC) over the total number of altered regions per anatomical cluster

Discussion

Thresholds sensitivity

With respect to wi-MC alterations, the selected threshold (97.5^{th} percentile) leads to Dice coefficient values ranging from 0.69 to 0.81 when compared with matrices from alternative thresholds, which implies high consistency among thresholds. Therefore, we opted for the 97.5^{th} percentile to minimize the occurrence of false positives. With respect to SUVR alterations, Dice coefficients between matrices derived from different thresholds are all above 0.86, suggesting that the choice of the threshold has limited influence on defining altered areas. To remain consistent with the wi-MC alteration choice, a threshold of 97.5% is chosen for determining SUVR alterations. Lastly, at identical thresholds, the Dice coefficient between MC and SUVR alteration matrices is consistently around 0.4-0.45, thus displaying limited threshold sensitivity.

SUVR impairments

We computed the Overall Impairment of SUVR and assessed its relationship with established markers of disease severity such as lesion grade and volume. While this index is capable of discriminating between low and high-grade patients, showing significantly lower values for the former, no relationship was found with lesion volume. Conversely, when analyzing the Overall Impairment estimated by wi-MC, a significant relationship not only with lesion grade but also with volume emerged. This highlights the higher sensitivity of this measure of metabolic connectome alteration compared to the more standard analysis using SUVR.

Impact of scanner and reconstruction algorithm

The Mann-Whitney U-test did not reveal any significant differences in the distribution of Contrast-to-Noise ratio (CNR) values between patients and controls ($P = 0.97$). This result gives confidence to the interpretation of the observed between-group differences (HCs and glioma patients) as physio-pathological alterations rather than as scanner and/or reconstruction-related artifacts.

References

[1] Goyal MS, Blazey T, Metcalf N V., et al. Brain aerobic glycolysis and resilience in Alzheimer disease. Proc Natl Acad Sci U S A. 2023;120(7):1–8. https://doi.org/10.1073/pnas.2212256120

[2] Elam JS, Glasser MF, Harms MP, et al. The Human Connectome Project: A retrospective. Neuroimage. 2021;244(May):118543. https://doi.org/10.1016/j.neuroimage.2021.118543

[3] Tustison NJ, Avants BB, Cook PA, et al. N4ITK: Improved N3 bias correction. IEEE Trans Med Imaging. 2010;29(6):1310–20.

[4] Doshi J et al. Multi-Atlas Skull-Stripping. Acad Radiol. 2013;20(12). https://www.ncbi.nlm.nih.gov/pmc/articles/PMC3624763/pdf/nihms412728.pdf

[5] Rousset O, Rahmim A, Alavi A, et al. Partial Volume Correction Strategies in PET. PET Clin. 2007;2(2):235–49.

[6] Avants BB, Tustison NJ, Song G, et al. A reproducible evaluation of ANTs similarity metric performance in brain image registration. Neuroimage. 2011;54(3):2033–44. http://dx.doi.org/10.1016/j.neuroimage.2010.09.025

[7] Hammers A, Allom R, Koepp MJ, et al. Three-dimensional maximum probability atlas of the human brain, with particular reference to the temporal lobe. Hum Brain Mapp. 2003;19(4):224–47. https://doi.org/10.1002/hbm.10123

[8] Yan X, Kong R, Xue A, et al. Homotopic local-global parcellation of the human cerebral cortex from resting-state functional connectivity. Neuroimage. 2023;273(October 2022):120010. https://doi.org/10.1016/j.neuroimage.2023.120010

[9] Andersen SM, Rapcsak SZ, Beeson PM. Cost function masking during normalization of brains with focal lesions: Still a necessity? Neuroimage. 2010;53(1):78–84. http://dx.doi.org/10.1016/j.neuroimage.2010.06.003

[10] Volpi T, Vallini G, Silvestri E, et al. A new framework for metabolic connectivity mapping using bolus [18 F]FDG PET and kinetic modelling. J Cereb Blood Flow Metab. 2022;1–21. https://doi.org/10.1177/0271678X231184365